Editors' Suggestion

Magneto-Seebeck microscopy of domain switching in collinear antiferromagnet CuMnAs

T. Janda,[1,2,*] J. Godinho,[3,1,*] T. Ostatnicky,[1] E. Pfitzner,[4] G. Ulrich,[5] A. Hoehl,[5] S. Reimers,[6] Z. Šobáň,[3] T. Metzger,[2] H. Reichlová,[7] V. Novák,[3] R. P. Campion,[6] J. Heberle,[4] P. Wadley,[6] K. W. Edmonds,[6] O. J. Amin,[6] J. S. Chauhan,[6] S. S. Dhesi,[8] F. Maccherozzi,[8] R. M. Otxoa,[9,10] P. E. Roy,[9] K. Olejník,[3] P. Němec,[1] T. Jungwirth,[3,6] B. Kaestner,[5,*] and J. Wunderlich[2,3,*]

[1]*Faculty of Mathematics and Physics, Charles University, Ke Karlovu 3, 121 16 Prague 2, Czech Republic*

[2]*Institute of Experimental and Applied Physics, University of Regensburg, Universitätsstraße 31, 93051 Regensburg, Germany*

[3]*Institute of Physics, Czech Academy of Sciences, Cukrovarnická 10, 162 00, Praha 6, Czech Republic*

[4]*Department of Physics, Freie Universität Berlin, 14195 Berlin, Germany*

[5]*Physikalisch-Technische Bundesanstalt, 38116 Braunschweig and 10587 Berlin, Germany*

[6]*School of Physics and Astronomy, University of Nottingham, Nottingham NG7 2RD, United Kingdom*

[7]*Institut fuer Festkoerper- und Materialphysik, Technische Universität Dresden, 01062 Dresden, Germany*

[8]*Diamond Light Source, Chilton, Didcot OX11 0DE, United Kingdom*

[9]*Hitachi Cambridge Laboratory, Cambridge CB3 0HE, United Kingdom*

[10]*Donostia International Physics Center, 20018 San Sebastián, Spain*

(Received 5 June 2020; accepted 12 August 2020; published 28 September 2020)

Antiferromagnets offer spintronic device characteristics unparalleled in ferromagnets owing to their lack of stray fields, THz spin dynamics, and rich materials landscape. Microscopic imaging of antiferromagnetic domains is one of the key prerequisites for understanding physical principles of the device operation. However, adapting common magnetometry techniques to the dipolar-field-free antiferromagnets has been a major challenge. Here we demonstrate in a collinear antiferromagnet a thermoelectric detection method by combining the magneto-Seebeck effect with local heat gradients generated by scanning far-field or near-field techniques. In a 20-nm epilayer of uniaxial CuMnAs we observe reversible 180° switching of the Néel vector via domain wall displacement, controlled by the polarity of the current pulses. We also image polarity-dependent 90° switching of the Néel vector in a thicker biaxial film, and domain shattering induced at higher pulse amplitudes. The antiferromagnetic domain maps obtained by our laboratory technique are compared to measurements by the established synchrotron-based technique of x-ray photoemission electron microscopy using x-ray magnetic linear dichroism.

DOI: 10.1103/PhysRevMaterials.4.094413

I. INTRODUCTION

Writing and reading by electrical and optical means, high-speed operation combined with neuromorphic memory characteristics, and novel topological phenomena are among the topics that have driven the research in the emerging field of antiferromagnetic spintronics [1–6]. The development of devices whose operation is based on antiferromagnets was initiated by theoretical predictions [7,8] and subsequent experimental demonstrations of electrical detection and manipulation of the antiferromagnetic order by relativistic anisotropic magnetoresistance (AMR) and Néel spin-orbit torque (NSOT) effects in metallic antiferromagnets [9–12]. From the early days of the antiferromagnetic spintronics research, special attention has been paid to complementing these electrical measurements by direct microscopic imaging of the typically multidomain states of the studied antiferromagnets [11,13–21]. The aim of these microscopies is to elucidate physical mechanisms of the switching which, e.g., in CuMnAs have been associated with the Néel vector reorientation induced by the NSOT, and with electrical or optical pulse-induced quenching into nanofragmented domain states of the antiferromagnet [20,21]. The microscopies are also essential for disentangling potential parasitic nonmagnetic contributions to the resistive switching signals, as reported in metal/antiferromagnetic-insulator bilayers [19,22–26].

However, established microscopy techniques for imaging antiferromagnets are rare and rely primarily on large-scale experimental facilities. Among these, x-ray magnetic linear dichroism combined with photoemission electron microscopy (XMLD-PEEM) [27] was used to visualize the electrical control of the Néel vector in CuMnAs, Mn_2Au, or NiO [11,13–15,18,19]. In CuMnAs, the XMLD-PEEM images of the onset of current-induced NSOT reorientation of the Néel vector were directly linked to the onset of the corresponding electrical readout signals due to AMR [13,14], and 90° Néel vector switching was observed by XMLD-PEEM for orthogonal writing currents [11,13] or, via domain wall motion, when reversing the polarity of the writing current [14]. Since XMLD-PEEM is a synchrotron-based technique, more accessible table-top microscopies are necessary for a systematic exploration of antiferromagnetic devices. An example here is the NV-diamond magnetometry [28,29] which was recently reported in antiferromagnetic Cr_2O_3, $BiFeO_3$, and CuMnAs [20,30,31], and which relies, however, on stray fields generated by uncompensated magnetic moments.

*Corresponding author.

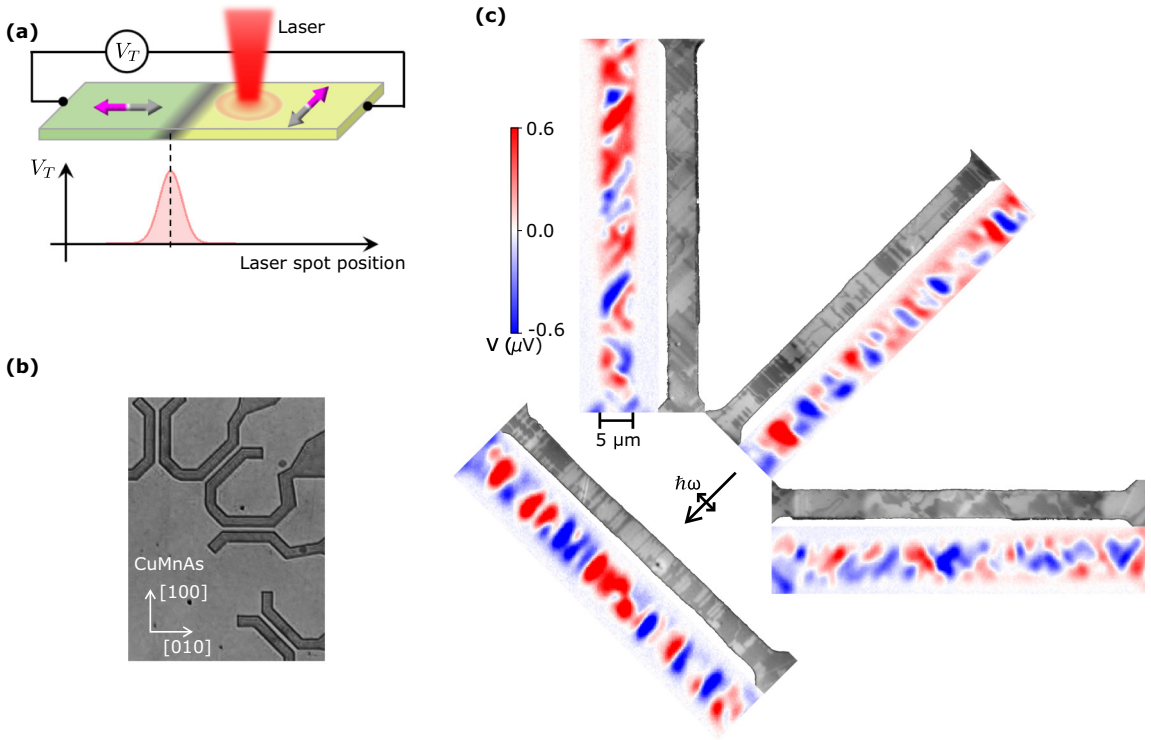

FIG. 1. Comparison between laboratory optical and synchrotron x-ray images of the domain structure in bar-shaped patterned antiferromagnetic CuMnAs. (a) Schematics of the measurement setup for the laboratory SFOM-MSE technique (top panel). A focused laser beam creates a local thermal gradient. When scanned over an antiferromagnetic (purple and gray arrows) texture, the in-plane components of the thermal gradient generate a voltage across the bar due to the MSE (bottom panel). (b) Optical micrograph of four 50-μm-long and 5-μm-wide bars patterned from a 45-nm-thick CuMnAs epilayer along [100], [1$\bar{1}$0], [110], and [010] crystallographic axes of CuMnAs. (c) Comparison between SFOM-MSE and XMLD-PEEM measurements in the four microbars. Antiferromagnetic domain structure is observed by XMLD-PEEM for x-ray polarization $E \parallel [1\bar{1}0]$ crystal axis. The single- and double-headed arrows in panel (c) indicate the in-plane projection of the x-ray propagation vector and the x-ray polarization vector, respectively. The light (dark) contrast corresponds to antiferromagnetic domains with the Néel vector oriented perpendicular (parallel) to the x-ray polarization.

In this work, we investigate current pulse-induced changes of the domain structure in the compensated collinear antiferromagnet CuMnAs [32,33], focusing on 90° and 180° Néel vector switching as well as domain fragmentation. For the microscopic imaging, we utilize a thermoelectric response due to the magneto-Seebeck effect (MSE), which is a thermal analog of AMR. The MSE can be applied to the large class of conductive antiferromagnets and is not limited to either uncompensated antiferromagnets that still produce detectable magnetic stray fields, or to systems whose additional broken symmetries allow for the anomalous Nernst effect or the magnetooptical Kerr effect, such as noncollinear antiferromagnets.

The MSE response is mapped to a laser-induced localized temperature gradient in the device. A thermoelectric voltage signal is measured across the entire bar device when the scanning probe is placed on top of an antiferromagnetic texture with spatially varying Néel vector.

We employ two techniques: The first one is based on the scanning far-field optical microscopy (SFOM) [34], which in combination with anomalous Nernst or spin-Seebeck thermoelectric response was employed in earlier studies of a noncollinear antiferromagnet Mn_3Sn and a metal/antiferromagnetic-insulator bilayer Pt/NiO, respectively [16,17]. In the second, high-resolution approach we utilize photocurrent nanoscopy in a scattering-type scanning near-field optical microscope (SNOM) [35–37]. Here a metal-coated tip of an atomic force microscope (AFM) placed in close proximity to the CuMnAs surface acts as an optical antenna for light focused on the tip. The incident electric field is strongly confined around the tip apex, providing a nanoscale near field point source. Since, to the best of our knowledge, the scanning optical microscopy combined with MSE has not been applied to antiferromagnets prior to our work, we provide comparisons to images obtained by the established synchrotron XMLD-PEEM technique.

II. COMPARISON OF OPTICAL-THERMOELECTRIC AND X-RAY MICROSCOPIES OF CUMNAS DOMAINS

In Fig. 1(a), we illustrate our SFOM-MSE technique on two neighboring antiferromagnetic domains separated by a 90° domain wall. We use a 800-nm wavelength cw-laser beam of 1 mW focused to a spot with a full-width at half-maximum (FWHM) of ≈1 μm on the surface of the CuMnAs antiferromagnet. The laser spot generates a lateral radially symmetric temperature gradient and we monitor the laser-induced thermoelectric voltage, V_T, at the two ends of the bar device. Nonzero V_T may occur when the temperature gradient crosses an antiferromagnetic domain boundary, as shown schematically in Fig. 1(a). This is because the Néel vector reorients

and, therefore, the magneto-Seebeck coefficient changes [38] so that the net thermoelectric signal does not cancel. As we show in the Supplemental Material [39], we can reproduce the sign and magnitude of the measured V_T signal with a magneto-Seebeck coefficient $\Delta S = S_c - S_p = 4\ \mu$V/K by considering the boundary conditions of our open circuit configuration, thermal conductivities of 200 W/(K m) and 75 W/(K m) for the metallic CuMnAs film and for the insulating GaP substrate, respectively, and by assuming that 50% of the laser power is absorbed within the metallic CuMnAs layer. Here, S_c (S_p) is the Seebeck coefficient when the Néel vector is collinear (perpendicular) to the temperature gradient. Note that the calculated maximum temperature rise at 5 mW laser power, the highest power used in our SFOM-MSE experiments, is not greater than 6 K [39]. We also verified that anisotropies of the conductivity, e.g., due to AMR, give a negligible contribution to the thermoelectric voltage signal.

The optical micrograph in Fig. 1(b) shows four 50-μm-long and 5-μm-wide bars, which were patterned from a 45-nm-thick CuMnAs/GaP epilayer [14,32] along [100], [1$\bar{1}$0], [110], and [010] crystallographic axes of CuMnAs. The SFOM-MSE signals of the four devices are compared in Fig. 1(c) to the XMLD-PEEM measurements taken on the same bars with x-ray polarization $E \parallel [1\bar{1}0]$ crystal axis. The light and dark areas correspond to antiferromagnetic domains with the Néel vector oriented perpendicular and parallel to the x-ray polarization, respectively [11,14]. Both domains with orthogonal orientation are found in our 45-nm-thick CuMnAs film with the dominant in-plane biaxial magnetic anisotropy [14].

The SFOM-MSE and the XMLD-PEEM measurements show analogous structures of micron-scale domains in each of the four bars. The preferential alignment of the domain walls follows the crystallographic directions of the in-plane square lattice of CuMnAs. This results in the 45° rotation of the preferred domain wall alignment with respect to the bar edges between the [100] ([010]) and [1$\bar{1}$0] ([110]) bars.

The analogous overall structure of the SFOM-MSE and XMLD-PEEM images confirms that the main contribution to the thermoelectric voltage signal comes from the antiferromagnetic texture and the corresponding variation of the magneto-Seebeck coefficient. Quantitative differences between the two measurements can be ascribed to different lateral resolution and depth sensitivity of the two techniques. The lateral resolution of the XMLD-PEEM in the metallic antiferromagnet CuMnAs is about 50 nm while the resolution of the SFOM-MSE is limited by the thermal gradient generated by the $\approx$ 1-μm-wide Gaussian shaped laser spot. Regarding the depth sensitivity, the photoelectrons in the XMLD-PEEM are detected only from a few-nm surface layer of the antiferromagnet while the thermoelectric measurements probe the full thickness of the antiferromagnetic film. Note also that the XMLD-PEEM measurements were performed about 10 days before the SFOM-MSE measurements.

III. OPTICAL THERMOELECTRIC IMAGING OF THE CURRENT-INDUCED SWITCHING

We now use the SFOM method to correlate the local magnetic domain structure to electrical resistance variation

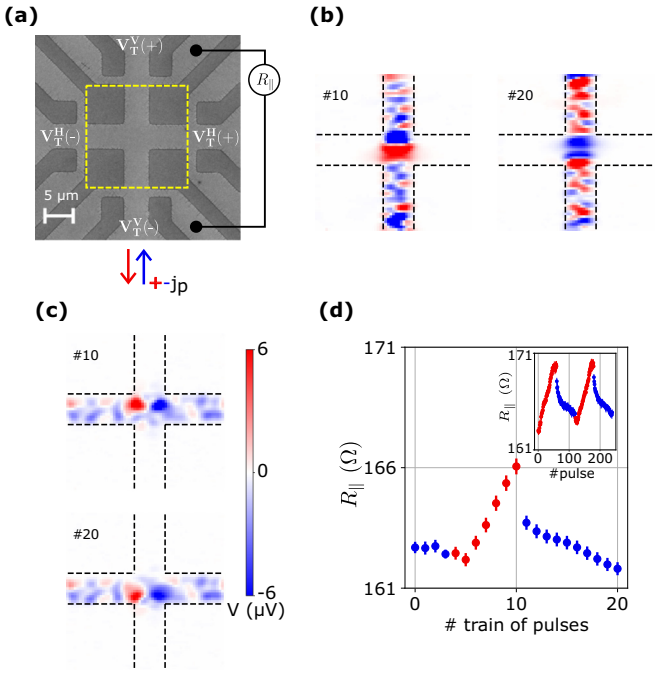

FIG. 2. Current-pulse-induced modification of the domain structure detected by MSE scans and compared to AMR measurements. (a) SEM micrograph of a 5-μm-wide cross bar patterned from a 45-nm-thick CuMnAs epilayer. The MSE scans have been performed within the area of 25 × 25 μm^2, indicated by the yellow dashed line. (b) MSE signal measured along the vertical bar after seven trains of positive pulses (left) followed by 10 trains of negative pulses (right). Each train of pulses contains six individual pulses. (c) MSE signal simultaneously measured along the horizontal bar. (d) Corresponding variation of the magnetoresistance measured in a four-point geometry along the vertical bar. Red (blue) data points correspond to resistance measurements after current pulses of positive (negative) polarity with $|j_p| = 9.6 \times 10^{10}$ A/m^2 and $\tau_p = 20$ ms.

after current pulse excitation, which further evidences that the image contrast we detect is indeed of magnetic origin. We simultaneously measure the thermoelectric signals along the vertical and horizontal bars in a symmetric 5-μm-wide cross bar geometry, shown in Fig. 2(a). The vertical and horizontal SFOM-MSE voltages $V_T^V = V_T^V(+) - V_T^V(-)$ and $V_T^H = V_T^H(+) - V_T^H(-)$ in Fig. 2(a) are recorded while scanning the focused laser spot over the central crossbar structure, highlighted in Fig. 2(a) by the dashed yellow rectangle.

Figures 2(b) and 2(c) show the corresponding maps after trains of positive and negative current pulses were applied along the vertical bar with amplitude $|j_p| = 9.6 \times 10^{10}$ A/m^2 and duration $\tau_p = 20$ ms. Vertical and horizontal thermoelectric signals reflect a complex microscopic domain structure. They appear only when the scanning laser spot illuminates the corresponding bars. After the applied vertical current pulses, variations of the vertical signal were observed along the entire vertical bar, whereas the horizontal signal changes only in the central overlapping crossbar region. These measurements confirm current-pulse-induced switching of the microscopic domain structure since modifications of the thermoelectric signal occur only in areas where the current density of the

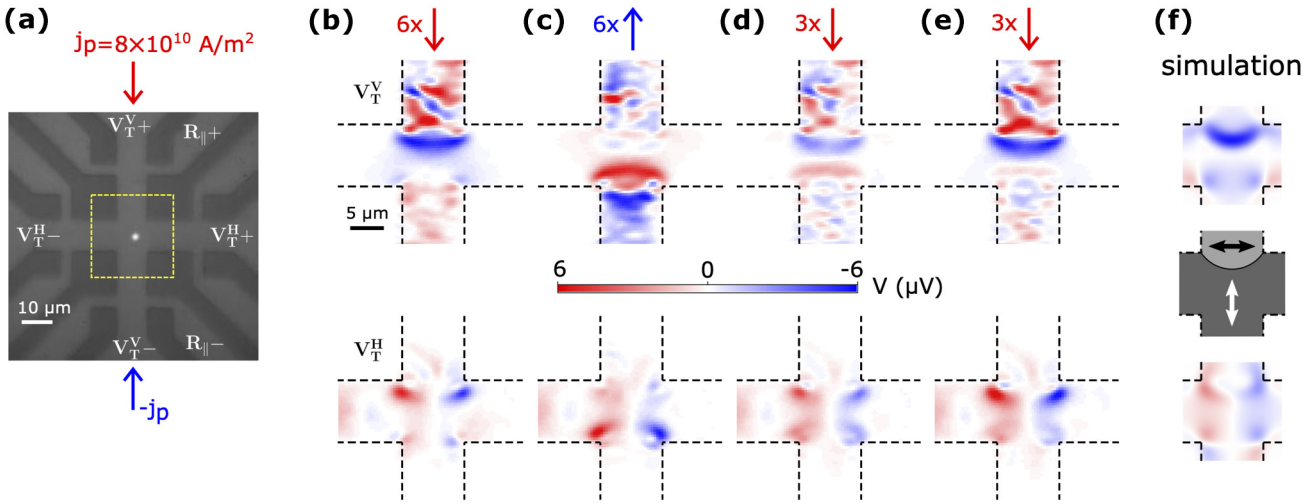

FIG. 3. Reproducibility of antiferromagnetic texture after pulsing with alternating polarity. (a) Optical micrograph of a 10-μm-wide cross bar, showing the measurement contacts geometry used. [(b)–(e)] Sequence of MSE maps of the vertical thermoelectric voltage and horizontal thermoelectric voltage measured simultaneously for alternating pulses. The MSE scans were performed within the area highlighted by the yellow dashed line in panel (a). (f) Simulated MSE maps of V_T^V (upper graph) and V_T^H (lower graph) for a domain configuration of a geometrically pinned domain wall (middle schematics) by taking into account the experimental conditions of a focused laser spot with Gaussian profile of 1.5-μm FWHM and 5-mW laser power and by assuming a magneto-Seebeck coefficient of $\Delta S = 4\ \mu\mathrm{V/K}$.

applied pulse was sufficiently large to trigger the switching [14].

Figure 2(d) shows the electrical resistance, $R_{||}$, measured in a four-point geometry after applying current pulses along the vertical bar. We found that variations in $R_{||}$ are accompanied with modified SFOM-MSE maps in Figs. 2(b) and 2(c), which are due to the current pulse-induced modification of the domain configuration in the current carrying bar. $R_{||}$ changes reversibly and reproducibly by applying pulses of opposite polarity, as shown in the inset of Fig. 2(d). This is consistent with the NSOT switching mechanism which was identified in the earlier XMLD-PEEM study at comparable amplitudes of the current pulses [14]. Note that we observe a change in resistance of about 4%. This is larger than the expected AMR due to 90° Néel vector reorientation inside a domain [14,40] and indicates that additional effects contribute to the variation of $R_{||}$ in our multidomain state.

To further evidence the reversible NSOT switching controlled by the current polarity, we measure a 10-μm-wide symmetric cross bar device, shown in Fig. 3(a). We start by applying six positive pulses along the vertical channel and record the SFOM-MSE map shown in Fig. 3(b). After applying six negative pulses, we obtain the significantly modified image shown in Fig. 3(c). When applying again six positive pulses, we recover the nearly identical original SFOM-MSE map [cf. Figs. 3(b) and 3(e)].

In Fig. 3(f), we simulate the SFOM-MSE measurement considering a realistic domain configuration. We compare the measurements shown in Figs. 3(b)–3(e) with results from self-consistent simulations of the MSE response for the vertical and horizontal bars of a geometrically pinned bubble-shape domain wall in a symmetric cross structure. We consider that due to the higher current density within the bar, domains with their Néel vector parallel to the NSOT driving field enlarge their size to gain the effective Zeeman energy [8]. The domain wall motion remains restricted by geometric pinning at the cross entrance when moving the domain wall toward the cross center [41,42]. The corresponding self-consistently calculated MSE maps for the vertical bar and the horizontal bar are in good qualitative agreement with our measurements. Details on the simulation as well as a discussion on the small AMR contributions to the thermoelectric signal can be found in the Supplemental Material [39].

So far, we have discussed SFOM-MSE experiments in which electrical pulses of opposite polarity caused reversible Néel vector switching via domain wall displacement in the antiferromagnet with micron-scale domains. When applying stronger pulses of amplitude $|j_p| = 1.3 \times 10^{11}\ \mathrm{A/m^2}$, we observe diminishing contrast of the SFOM-MSE signal, as shown in Figs. 4(a) and 4(b) for a 5-μm-wide bar. We ascribe the vanishing SFOM-MSE contrast to a fragmented multidomain state of the antiferromagnet with submicron feature sizes that are significantly smaller than the extension of the thermal gradient in our SFOM experiment. As a consequence, the net thermoelectric signal from the many domains averages out. Acquiring the full SFOM-MSE image after the pulse takes about 30 min. For comparison, we show in Figs. 4(d)–4(f) XMLD-PEEM measurements on a similar CuMnAs film and with similar pulse amplitudes, taken a few minutes after the pulse [Fig. 4(e)] and again after 4 h [Fig. 4(f)]. We see that domains are shattered into a fragmented state with many small submicron domains by the current pulse, consistent with the SFOM image in Fig. 4(b). The large domains on the left and right side of the horizontal channel remained unaffected since they were not exposed to the current pulse. The domain fragmentation in CuMnAs has been explored in parallel XMLD-PEEM and NV-diamond imaging studies and associated with quenched metastable states which form after pulse-heating the system close to the Néel temperature [20,21]. Systematic electrical readout measurements showed that corresponding resistive switching signals can reach giant-magnetoresistance amplitudes of ≈10–100%, i.e., far exceed

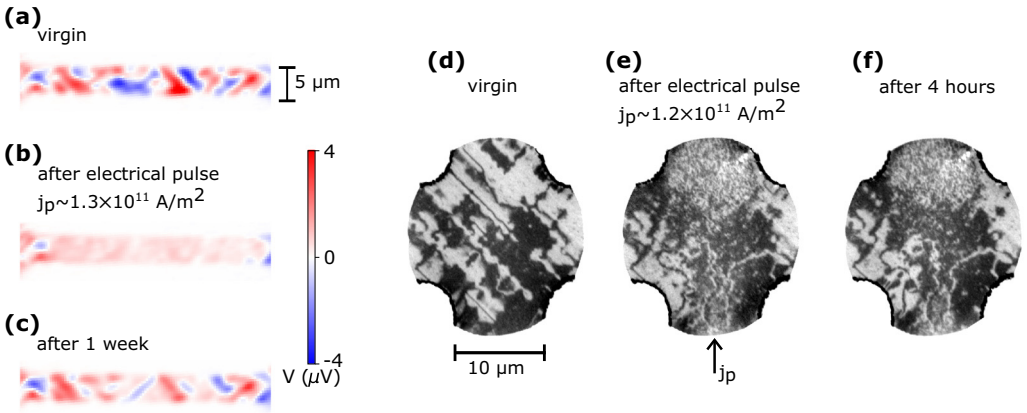

FIG. 4. Shattering of magnetic domains after an electrical pulse. (a) SFOM-MSE scan of a 5-μm-wide bar device prior to any electrical pulse. (b) After a pulse with a current density of 1.3×10^{11} A/m^2, the contrast is lost with the main features absent. The loss of contrast is ascribed to the shattering of the magnetic domains into smaller domains, which become significantly smaller than the spatial resolution of the SFOM-MSE. Hence, the total SFOM-MSE signal over many domain walls averages nearly to zero. (c) The SFOM-MSE signal 1 week after the electrical pulse, where a similar pattern of large domains has reappeared and is resembling the initial state in panel (a). (d) XMLD-PEEM measurements prior the pulse, (e) just after the pulse with a current density of 1.2×10^{11} A/m^2, and (f) 4 h after the pulse.

the signals associated with NSOT-induced Néel vector reorientations in the unshattered state with domain sizes in the micron-scale or larger [20,21].

Our laboratory SFOM-MSE technique allows for exploring the relaxation of the metastable fragmented states over long timescales. Remarkably, when remeasuring the SFOM-MSE signal 1 week after the pulse, we find again large-scale SFOM-MSE pattern which resembles the original pattern measured prior to the applied pulse [cf. Figs. 4(a) and 4(c)]. This observation, consistent with the results of the NV-diamond imaging [20], hints to the presence of nucleation and pinning centers in the CuMnAs film. On the other hand, we also note that the disappearance of the contrast observed in the SFOM-MSE measurements in short times after the pulse confirm that potential nonmagnetic thermoelectric contributions from defects are small compared to the MSE signal from the antiferromagnetic domains.

The interpretation of the SFOM-MSE signal in terms of an actual domain structure may only be justified for sizes larger than the spatial resolution, as highlighted in Figs. 3(b)–3(e). However, the feature sizes can be significantly smaller [20,21] [see also Figs. 4(e) and 4(f)]. In the following, we introduce a high-resolution method where we can resolve narrow 180° antiferromagnetic domain walls in a thin CuMnAs film with uniaxial magnetic anisotropy, and observe polarity-dependent 180° switching via domain wall displacement.

IV. HIGH-RESOLUTION IMAGING OF CURRENT-INDUCED DISPLACEMENT OF 180° DOMAIN WALLS

CuMnAs films of thickness $\leqslant$20 nm exhibit a dominant uniaxial magnetic anisotropy component ascribed to the symmetry breaking between the GaP [110] and [1$\bar{1}$0] axes (CuMnAs [100] and [010] axes) at the GaP/CuMnAs interface [33,40,43]. In such films, narrow 180° domain walls separate magnetic domains with reversed Néel vectors as shown, e.g., by XMLD-PEEM measurements on a 10-nm CuMnAs film in the Supplemental Material [39].

In the following, we present MSE measurements on bar devices patterned from a 20-nm CuMnAs film. (For further discussion of the uniaxial anisotropy in this film as confirmed by our MSE measurements, see the Supplemental Material [39].) The detectable MSE signal in uniaxial films is generated only within the 180° antiferromagnetic domain wall since the two neighboring domains with opposite Néel vectors share the same Seebeck coefficient. In order to image narrow 180° domain walls, we therefore have to generate a thermal gradient with spatial resolution of the order of the domain wall width. To enhance the spatial resolution, we scatter the laser light from a metallic tip, as known from scattering-type SNOM [44]. This technique allows us to focus light on a spot size of a few tens of nm, only limited by the tip's dimensions [45], and hence to generate a much sharper thermal gradient as compared to the SFOM method.

In Fig. 5(a), we illustrate our SNOM-MSE technique. The radiation-induced temperature profile underneath the tip is indicated by the red spot. The MSE signal appears as two features of the same intensity but opposite polarity when scanning with the AFM tip over the 180° domain wall, since only the variation of the magneto-Seebeck coefficient within the domain wall contributes to the signal. The position where the MSE signal switches sign therefore corresponds to the position of the 180° domain wall.

Figure 5(b) shows a micrograph of a 2-μm-wide CuMnAs bar device below the cantilever with the AFM tip. The thermoelectric voltage, V_T, generated in the channel is analyzed by a lock-in amplifier at the AFM tip modulation frequency Ω. For tip-enhanced focusing, we use a scattering-type SNOM operated in the tapping mode. A gold-coated Si cantilever with a typical tip diameter of less than 50 nm oscillates with an amplitude of 80 nm above the sample surface at its mechanical resonance frequency $\Omega \approx 240$ kHz. The continuous wave emission of a quantum cascade laser is focused onto the tip apex which acts as an antenna transmitting a

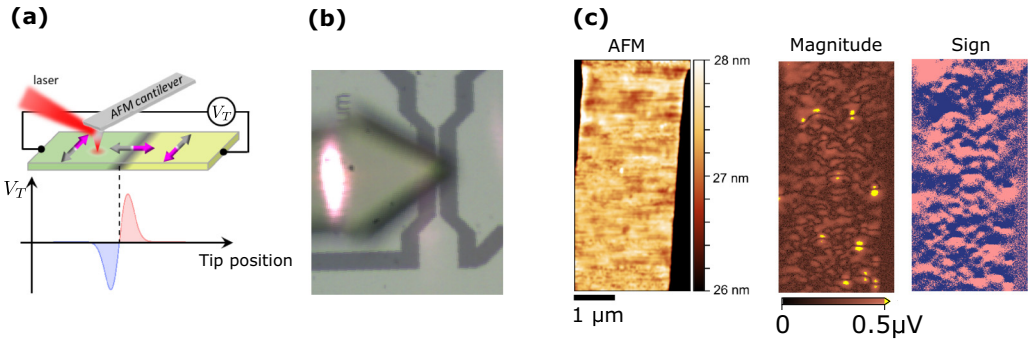

FIG. 5. SNOM-MSE scan of a bar device patterned from a uniaxial CuMnAs layer. (a) Schematics of the SNOM-MSE setup. The thermal gradient is created when a metal-coated AFM tip interacts with an infrared laser, inducing an optical near field at the apex of the tip. A 180° domain wall appears in the MSE maps as two features of opposite sign together, as illustrated in the bottom panel. (b) Micrograph of the scanned bar-device, where the AFM tip is also visible. (c) From left to right: topography map, magnitude of the MSE signal, and its sign.

strongly confined near field to the sample surface. In contrast to our diffraction-limited SFOM method with $\lambda = 800$ nm excitation wavelength, we use here a laser emission with mid-infrared wavelength because the longer wavelength couples more efficiently into the AFM tip and the resolution of this near-field method is not diffraction limited.

Figure 5(c) shows, from left to right, the AFM topography image, the magnitude of the thermoelectric voltage $|V_T|$, and its sign $sgn(V_T)$, all detected simultaneously during the SNOM-MSE measurement. As evident from the comparison between the SNOM-MSE signal and the AFM topography, the majority of the features appearing in the MSE map do not correlate with defects in the topography. We therefore conclude that also in this uniaxial material the contrast originates dominantly from the antiferromagnetic texture. In order to highlight the position of the 180° domain walls, we plot the absolute value of the measured signal alongside with its polarity. We can then identify the 180° domain walls as meandering zero-signal lines that surround micron-size antiferromagnetic domains.

In order to investigate the effect of current-induced NSOT on the 180° domain walls, we manipulate the magnetic texture by sending current pulses through the bar device, as illustrated in Fig. 6. We apply current pulses of $|j_p| \approx 2.5 \times 10^{11}$ A/m^2 with a duration of 1 ms and with alternating polarity in order to illustrate the reversible switching; the current direction is shown by the red and blue arrows. Note that the onset current amplitude for switching in the 20 nm CuMnAs film is higher than in the above switching experiments in the 45-nm film. We do not attribute it to the difference of intrinsic properties of the two films. It results from the heat-assisted nature of switching [21,46] and from an interplay of device geometry and heat dissipation during the writing pulse. For ultrashort pulses (with lengths in the ns scale or smaller), the temperature increase of the CuMnAs device is determined by the energy density delivered by the pulse. Hence, the onset current density for switching does not depend on the dimensions of the CuMnAs device [46]. For longer pulses, including those used in the present work, the effect of heat dissipation from the device during the pulse becomes important. Consequently, the current density required to achieve the same switching temperature increases with decreasing film thickness.

In Figs. 6(a) and 6(b), we plot enlargements of the measured $|V_T|$ and $sgn(V_T)$ after applying a train of 22 current pulses before applying the train of current pulses again with opposite polarity. We found that depending on the polarity of the applied pulses, the antiferromagnetic domains change their size by reversibly displacing domain walls, consistent with the NSOT driven antiferromagnetic domain wall motion [47,48]. We also identify areas in which antiferromagnetic domains merge with or separate from neighboring domains depending on the current pulse polarity. A possible explanation for this observation are intrinsic crystal defects such as slip dislocation antiphase boundary defects and microtwin

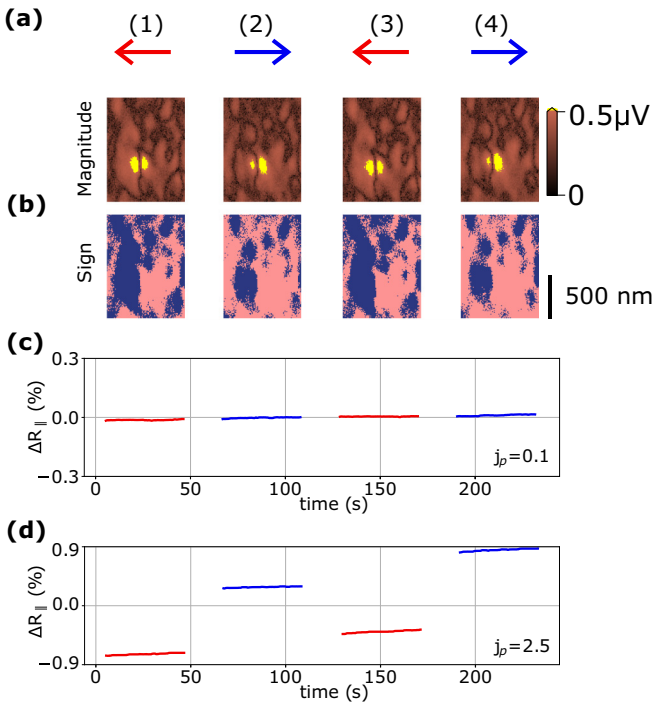

FIG. 6. Reversible switching measured in SNOM-MSE. (a) Maps of the magnitude of the MSE signal, $|V_T|$, after applying current pulses of amplitude $|j_p| = 2.5 \times 10^{11}$ A/m^2 in opposite directions indicated by the red and blue arrow on top. (b) Maps of the corresponding $sgn(V_T)$ values. [(c), (d)] Resistance variations associated with the corresponding switching states for low and high current densities. Current density values shown are in 10^{11} A/m^2.

defects which are present in our thin epitaxial CuMnAs films [49] and which may act as domain wall pinning, nucleation, and annihilation centers similar to crystal defects in epitaxial ferromagnetic films [50].

The corresponding resistance changes are plotted in Figs. 6(c) and 6(d). After applying pulses of amplitude $|j_p| = 2.5 \times 10^{11}$ A/m^2, we observe in Fig. 6(d) bistable changes of the bar resistance of the order of 1–2%. In comparison, no changes are observed for $|j_p| = 0.1 \times 10^{11}$ A/m^2, as shown in Fig. 6(c). We attribute the resistance variations to magnetic scattering on the domain walls; the AMR contributions from the antiferromagnetic domains can be excluded in the uniaxial film. More details on the switching as a function of the polarity, number, and amplitude of the current pulses by means of principal components analysis can be found in the Supplemental Material [39].

V. CONCLUSIONS

We have introduced a laboratory method for imaging antiferromagnetic domain structure by mapping the local magneto-Seebeck effect using a far-field or near-field optical scanning approach. In uniaxial CuMnAs, we identify narrow 180° domain walls of submicron width and their pulse-induced displacements. These reversible, polarity-dependent modifications of the antiferromagnetic domain maps are consistent with the current-induced NSOT switching mechanism. We link the imaged domain changes to resistive switching signals which we attribute to scattering on the 180° domain walls. In biaxial CuMnAs, we confirm large micron-size domains and their current-pulse-induced modifications. We conclude that AMR from the 90° Néel vector reorientation in the antiferromagnetic domains can explain only part of the measured resistance variations. We suggest that magnetic scattering on domain walls gives a strong additional contribution to the observed resistive switching. Apart from the polarity-dependent NSOT reorientation of the Néel vector at lower pulse amplitudes, we also confirm shattering into fragmented metastable multidomain states with submicron feature sizes after applying larger amplitude pulses, and the subsequent relaxation toward the prepulsed state of the antiferromagnet.

ACKNOWLEDGMENTS

B.K., A.H., and G.U. acknowledge funding from the EMPIR programme (JRP ADVENT) cofinanced by the Participating States and from the European Union's Horizon 2020 research and innovation programme. E.P. and J.H. acknowledge funding from the DFG-project HE 2063/5-1. T.J., J.G., Z.S., H.R., V.N., K.O., J.W., and T.J. acknowledge funding from Ministry of Education of the Czech Republic Grant No. LM2018110 and LNSM-LNSpin, the Czech Science Foundation Grant No. 19-28375X, and the EU FET Open RIA Grant No. 766566. J.G., V.N., K.O., and J.W. acknowledge funding from the ERC Synergy Grant No. 610115. We acknowledge Diamond Light Source for time on Beamline I06 under Proposals No. SI16376 and No. SI20793.

T.J., P.N., and J.W. planned and prepared the SFOM-MSE measurements, which T.J. and J.G. carried out. G.U., E.P., A.H., and B.K. planned and prepared the SNOM-MSE measurements, which J.W., G.U., E.P., A.H., J.G., H.R., T.M., and B.K. carried out. J.G., H.R., J.W., and K.O. planned and performed the electrical pulsing experiments. S.R., O.J.A., J.S.C., P.W., K.W.E., S.S.D., and F.M. planned and performed the XMLD-PEEM measurements. T.O. performed the simulations. V.N., R.P.C., and P.W. grew and characterized the CuMnAs films. Z.S. designed and fabricated the devices. J.W., B.K., J.G., T.J., T.O., T.M., E.P., and T.J. wrote the paper. All authors discussed the results and contributed to the paper. B.K. and J.W. conceived and planned the study.

APPENDIX: METHODS

1. Sample fabrication

For patterning our samples, we used standard electron beam lithography on an polymethyl methacrylate (PMMA) resist film after cleaning the surface of our CuMnAs wafers with acetone. After removing the Al/AlO_x capping layer using diluted Tetramethylammoniumhydroxid (TMAH) developer, the individual devices were defined by etching insulating trenches using a mixture of H_2SO_4, $C_4H_6O_6$, H_2O_2, and deionized H_2O. Bonding contacts were made using a lift-off process following the Cr(3 nm)-Au(80 nm) evaporation.

2. SFOM-MSE technique

The laser beam emitted by a Ti:sapphire continuous-wave (cw) laser (Spectra Physics, model 3900S) tuned to a wavelength of 800 nm was focused into a spot size of $\approx$1.5 μm full width at half maximum (FWHM) by an objective lens (Mitutoyo Plan Apo 20). The data in Fig. 1 were measured with a laser power of 1 mW and the data in Figs. 2–4 with a power of 5 mW. Since the MSE signal is linear in the laser power (as confirmed by a test measurement, not shown here), the only effect of a larger laser power is a correspondingly larger MSE voltage and a higher signal-to-noise ratio. Scanning of the laser spot across the sample surface is achieved by moving the objective lens with a 3D piezo-positioner (Newport, NPXYZ100SG-D). The laser beam is modulated at a frequency of $\Omega \approx 1.7$ kHz by an optical chopper and from the measured and amplified MSE voltage the signal component at the chopper-frequency is extracted by a lock-in amplifier.

3. SNOM-MSE technique

The emission of a quantum cascade laser (QCL, 28 mW at $\lambda \approx 10\,\mu$m, MIRcat, Daylight Solutions Inc., CA, USA) was focused onto the metallic tip apex of the metal-coated Si cantilever (neaspec nano-FTIR scanning probes). Focusing and scanning of the tip were performed using a commercial scattering-type scanning near-field optical microscopy instrument (Neasnom, by Neaspec GmbH). The tip-mediated electric response of the sample was amplified by low-noise voltage preamplifier (Stanford Research SR 560, gain $= 5 \times 10^3$), and further demodulated at the tip-modulation frequency Ω and its higher harmonics with the lock-in amplifier of the Neasnom instrument. Both amplitude and phase were recorded while scanning the sample surface.

[1] T. Jungwirth, X. Marti, P. Wadley, and J. Wunderlich, Nat. Nanotechnol. **11**, 231 (2016).

[2] V. Baltz, A. Manchon, M. Tsoi, T. Moriyama, T. Ono, and Y. Tserkovnyak, Rev. Mod. Phys. **90**, 015005 (2018).

[3] J. Železný, P. Wadley, K. Olejník, A. Hoffmann, and H. Ohno, Nat. Phys. **14**, 220 (2018).

[4] O. Gomonay, V. Baltz, A. Brataas, and Y. Tserkovnyak, Nat. Phys. **14**, 213 (2018).

[5] P. Němec, M. Fiebig, T. Kampfrath, and A. V. Kimel, Nat. Phys. **14**, 229 (2018).

[6] L. Šmejkal and T. Jungwirth, in *Topology in Magnetism*, edited by J. Zang, V. Cros, and A. Hoffmann (Springer International, Berlin, 2018), pp. 267–298.

[7] A. B. Shick, S. Khmelevskyi, O. N. Mryasov, J. Wunderlich, and T. Jungwirth, Phys. Rev. B **81**, 212409 (2010).

[8] J. Železný, H. Gao, K. Výborný, J. Zemen, J. Mašek, A. Manchon, J. Wunderlich, J. Sinova, and T. Jungwirth, Phys. Rev. Lett. **113**, 157201 (2014).

[9] B. G. Park, J. Wunderlich, X. Martí, V. Holý, Y. Kurosaki, M. Yamada, H. Yamamoto, A. Nishide, J. Hayakawa, H. Takahashi, A. B. Shick, and T. Jungwirth, Nat. Mater. **10**, 347 (2011).

[10] X. Marti, I. Fina, C. Frontera, J. Liu, P. Wadley, Q. He, R. J. Paull, J. D. Clarkson, J. Kudrnovský, I. Turek, J. Kuneš, D. Yi, J.-H. Chu, C. T. Nelson, L. You, E. Arenholz, S. Salahuddin, J. Fontcuberta, T. Jungwirth, and R. Ramesh, Nat. Mater. **13**, 367 (2014).

[11] P. Wadley, B. Howells, J. Železný, C. Andrews, V. Hills, R. P. Campion, V. Novák, K. Olejník, F. Maccherozzi, S. S. Dhesi, S. Y. Martin, T. Wagner, J. Wunderlich, F. Freimuth, Y. Mokrousov, J. Kuneš, J. S. Chauhan, M. J. Grzybowski, A. W. Rushforth, K. Edmond *et al.*, Science **351**, 587 (2016).

[12] J. Godinho, H. Reichlova, D. Kriegner, V. Novak, K. Olejnik, Z. Kaspar, Z. Soban, P. Wadley, R. P. Campion, R. M. Otxoa, P. E. Roy, J. Zelezny, T. Jungwirth, and J. Wunderlich, Nat. Commun. **9**, 4686 (2018).

[13] M. J. Grzybowski, P. Wadley, K. W. Edmonds, R. Beardsley, V. Hills, R. P. Campion, B. L. Gallagher, J. S. Chauhan, V. Novak, T. Jungwirth, F. Maccherozzi, and S. S. Dhesi, Phys. Rev. Lett. **118**, 057701 (2017).

[14] P. Wadley, S. Reimers, M. J. Grzybowski, C. Andrews, M. Wang, J. S. Chauhan, B. L. Gallagher, R. P. Campion, K. W. Edmonds, S. S. Dhesi, F. Maccherozzi, V. Novak, J. Wunderlich, and T. Jungwirth, Nat. Nanotechnol. **13**, 362 (2018).

[15] T. Moriyama, K. Oda, T. Ohkochi, M. Kimata, and T. Ono, Sci. Rep. **8**, 14167 (2018).

[16] H. Reichlova, T. Janda, J. Godinho, A. Markou, D. Kriegner, R. Schlitz, J. Zelezny, Z. Soban, M. Bejarano, H. Schultheiss, P. Nemec, T. Jungwirth, C. Felser, J. Wunderlich, and S. T. B. Goennenwein, Nat. Commun. **10**, 5459 (2019).

[17] I. Gray, T. Moriyama, N. Sivadas, G. M. Stiehl, J. T. Heron, R. Need, B. J. Kirby, D. H. Low, K. C. Nowack, D. G. Schlom, D. C. Ralph, T. Ono, and G. D. Fuchs, Phys. Rev. X **9**, 041016 (2019).

[18] S. Y. Bodnar, M. Filianina, S. P. Bommanaboyena, T. Forrest, F. Maccherozzi, A. A. Sapozhnik, Y. Skourski, M. Kläui, and M. Jourdan, Phys. Rev. B **99**, 140409(R) (2019).

[19] L. Baldrati, O. Gomonay, A. Ross, M. Filianina, R. Lebrun, R. Ramos, C. Leveille, F. Fuhrmann, T. R. Forrest, F. Maccherozzi, S. Valencia, F. Kronast, E. Saitoh, J. Sinova, and M. Kläui, Phys. Rev. Lett. **123**, 177201 (2019).

[20] M. S. Wörnle, P. Welter, Z. Kašpar, K. Olejník, V. Novák, R. P. Campion, P. Wadley, T. Jungwirth, C. L. Degen, and P. Gambardella, arXiv:1912.05287.

[21] Z. Kašpar, M. Surýnek, J. Zubáč, F. Krizek, V. Novák, R. P. Campion, M. S. Wörnle, P. Gambardella, X. Marti, P. Němec, P. Wadley, J. Wunderlich, T. Jungwirth, and K. Olejník, arXiv:1909.09071.

[22] C. C. Chiang, S. Y. Huang, D. Qu, P. H. Wu, and C. L. Chien, Phys. Rev. Lett. **123**, 227203 (2019).

[23] B. Zink, Physics **12**, 134 (2019).

[24] P. Zhang, J. Finley, T. Safi, and L. Liu, Phys. Rev. Lett. **123**, 247206 (2019).

[25] Y. Cheng, S. Yu, M. Zhu, J. Hwang, and F. Yang, Phys. Rev. Lett. **124**, 027202 (2020).

[26] A. Churikova, D. Bono, B. Neltner, A. Wittmann, L. Scipioni, A. Shepard, T. Newhouse-Illige, J. Greer, and G. S. D. Beach, Appl. Phys. Lett. **116**, 022410 (2020).

[27] A. Scholl, Science **287**, 1014 (2000).

[28] C. L. Degen, Appl. Phys. Lett. **92**, 243111 (2008).

[29] G. Balasubramanian, I. Y. Chan, R. Kolesov, M. Al-Hmoud, J. Tisler, C. Shin, C. Kim, A. Wojcik, P. R. Hemmer, A. Krueger, T. Hanke, A. Leitenstorfer, R. Bratschitsch, F. Jelezko, and J. Wrachtrup, Nature (London) **455**, 648 (2008).

[30] T. Kosub, M. Kopte, R. Hühne, P. Appel, B. Shields, P. Maletinsky, R. Hübner, M. O. Liedke, J. Fassbender, O. G. Schmidt, and D. Makarov, Nat. Commun. **8**, 13985 (2017).

[31] I. Gross, W. Akhtar, A. Hrabec, J. Sampaio, L. J. Martínez, S. Chouaieb, B. J. Shields, P. Maletinsky, A. Thiaville, S. Rohart, and V. Jacques, Phys. Rev. Mater. **2**, 024406 (2018).

[32] P. Wadley, V. Novák, R. P. Campion, C. Rinaldi, X. Martí, H. Reichlová, J. Železný, J. Gazquez, M. A. Roldan, M. Varela, D. Khalyavin, S. Langridge, D. Kriegner, F. Máca, J. Mašek, R. Bertacco, V. Holý, A. W. Rushforth, K. W. Edmonds, B. L. Gallagher *et al.*, Nat. Commun. **4**, 2322 (2013).

[33] P. Wadley, V. Hills, M. R. Shahedkhah, K. W. Edmonds, R. P. Campion, V. Novák, B. Ouladdiaf, D. Khalyavin, S. Langridge, V. Saidl, P. Nemec, A. W. Rushforth, B. L. Gallagher, S. S. Dhesi, F. Maccherozzi, J. Železný, and T. Jungwirth, Sci. Rep. **5**, 17079 (2015).

[34] M. Weiler, M. Althammer, F. D. Czeschka, H. Huebl, M. S. Wagner, M. Opel, I. M. Imort, G. Reiss, A. Thomas, R. Gross, and S. T. B. Goennenwein, Phys. Rev. Lett. **108**, 106602 (2012).

[35] E. Pfitzner, X. Hu, H. W. Schumacher, A. Hoehl, D. Venkateshvaran, M. Cubukcu, J. W. Liao, S. Auffret, J. Heberle, J. Wunderlich, and B. Kästner, AIP Adv. **8**, 125329 (2018).

[36] A. Woessner, P. Alonso-González, M. B. Lundeberg, Y. Gao, J. E. Barrios-Vargas, G. Navickaite, Q. Ma, D. Janner, K. Watanabe, A. W. Cummings, T. Taniguchi, V. Pruneri, S. Roche, P. Jarillo-Herrero, J. Hone, R. Hillenbrand, and F. H. Koppens, Nat. Commun. **7**, 10783 (2016).

[37] M. B. Lundeberg, Y. Gao, A. Woessner, C. Tan, P. Alonso-González, K. Watanabe, T. Taniguchi, J. Hone, R. Hillenbrand, and F. H. Koppens, Nat. Mater. **16**, 204 (2017).

[38] P. Krzysteczko, X. Hu, N. Liebing, S. Sievers, and H. W. Schumacher, Phys. Rev. B **92**, 140405(R) (2015).

[39] See Supplemental Material at http://link.aps.org/supplemental/10.1103/PhysRevMaterials.4.094413 for more details on the simulation and other thermocurrent contributions, as well as a principal components analysis quantifying the domain wall motion.

[40] M. Wang, C. Andrews, S. Reimers, O. J. Amin, P. Wadley, R. P. Campion, S. F. Poole, J. Felton, K. W. Edmonds, B. L. Gallagher, A. W. Rushforth, O. Makarovsky, K. Gas, M. Sawicki, D. Kriegner, J. Zubáč, K. Olejník, V. Novák, T. Jungwirth, M. Shahrokhvand, U. Zeitler, S. S. Dhesi, and F. Maccherozzi, Phys. Rev. B **101**, 094429 (2020).

[41] J. Wunderlich, D. Ravelosona, C. Chappert, F. Cayssol, V. Mathet, J. Ferre, J.-P. Jamet, and A. Thiaville, IEEE Trans. Mag. **37**, 2104 (2001).

[42] T. Janda, P. E. Roy, R. M. Otxoa, Z. Šobáň, A. Ramsay, A. C. Irvine, F. Trojanek, M. Surýnek, R. P. Campion, B. L. Gallagher, P. Němec, T. Jungwirth, and J. Wunderlich, Nat. Commun. **8**, 15226 (2017).

[43] V. Saidl, P. Němec, P. Wadley, V. Hills, R. P. Campion, V. Novák, K. W. Edmonds, F. Maccherozzi, S. S. Dhesi, B. L. Gallagher, F. Trojánek, J. Kuneš, J. Železný, P. Malý, and T. Jungwirth, Nat. Photon. **11**, 91 (2017).

[44] F. Keilmann and R. Hillenbrand, Philos. Trans. R. Soc. London A **362**, 787 (2004).

[45] S. Mastel, A. A. Govyadinov, C. Maissen, A. Chuvilin, A. Berger, and R. Hillenbrand, ACS Photon. **5**, 3372 (2018).

[46] K. Olejník, T. Seifert, Z. Kašpar, V. Novák, P. Wadley, R. P. Campion, M. Baumgartner, P. Gambardella, P. Němec, J. Wunderlich, J. Sinova, P. Kužel, M. Müller, T. Kampfrath, and T. Jungwirth, Sci. Adv. **4**, eaar3566 (2018).

[47] O. Gomonay, T. Jungwirth, and J. Sinova, Phys. Rev. Lett. **117**, 017202 (2016).

[48] R. M. Otxoa, P. E. Roy, R. Rama-Eiroa, K. Y. Guslienko, and J. Wunderlich, arXiv:2002.03332.

[49] F. Krizek, Z. Kašpar, A. Vetushka, D. Kriegner, E. M. Fiordaliso, J. Michalicka, O. Man, J. Zubáč, M. Brajer, V. A. Hills, K. W. Edmonds, P. Wadley, R. P. Campion, K. Olejník, T. Jungwirth, and V. Novák, Phys. Rev. Mater. **4**, 014409 (2020).

[50] R. P. Cowburn, J. Ferré, S. J. Gray, and J. A. C. Bland, Phys. Rev. B **58**, 11507 (1998).